PAPER

Check for updates

Manipulating the mesostructure of silicoaluminophosphate SAPO-11 *via* tumbling-assisted, oriented assembly crystallization: a pathway to enhance selectivity in hydroisomerization†

Dongliang Jin,[ab] Liyuan Li,[c] Guanghua Ye,[ad] Hongxin Ding, [iD][a] Xiaoling Zhao,[a] Kake Zhu, [iD]*[a] Marc-Olivier Coppens [iD]*[d] and Xinggui Zhou[a]

Controlling the architecture of crystalline materials *via* a non-classical crystallization pathway provides a versatile route to optimise their properties. It is shown how a designed hierarchical architecture of silicoaluminophosphate SAPO-11 can be obtained by controlling the crystallization process, and how this affects hydroisomerization of *n*-heptane. Oriented attachment is identified as the main crystallization pathway when pre-fabricated nanocrystallites are used as precursors. Tumbling crystallization facilitates the in-plane alignment of nanocrystallites to afford a house-of-cards architecture, consisting of *ca.* 300 nm nanosheets along the same crystallographic *b* axis, while static crystallization only affords randomly oriented agglomerates made up of fused nanocrystallites. Using a growth modifier, cellulose 2-(2-hydroxy-3-(trimethylammonium)propoxy) ethyl ether chloride (polyquaternium-10 or PQ-10), reduces the lateral size of these platelets down to *ca.* 20 nm, while simultaneously increasing the auxiliary porosity and surface area, as well as the mass transfer properties of the hierarchically structured material. The preparation factors that influence the morphology of the final crystalline products can be associated with changes in interparticle interactions. A suite of characterization techniques, such as XRD, N_2 physisorption, Hg porosimetry, SEM, TEM, ^{28}Al, ^{31}P and ^{29}Si MAS NMR, NH_3-TPD and Py-IR were employed to elucidate the structure and acidity. Catalytic hydroisomerization tests for *n*-heptane demonstrate that the selectivity to isomerized components is governed by diffusion properties that rely on a hierarchical architecture. Hydroisomerization is the main reaction pathway only when operated within the diffusion controlled regime. Our findings thus provide more insight into how the hierarchical architecture of a catalyst influences the reaction product distribution.

Introduction

Zeotype materials are a class of inorganic solids that are made up of corner-sharing O vertices between neighbouring tetrahedral TO_4 (T = Si, Al, P, *etc.*) units that construct crystallographically well defined micropores with distinct dimen-

sions, shapes, intersections and connectivity.[1,2] They are traditionally used as ion-exchangers, adsorbents, acid catalysts or catalyst supports. In addition, their applications are expanding into other fields, such as imaging tracer, light-emitting, electronic or medical materials, and, henceforth, wider use may be anticipated.[3] As the micropore dimensions match those of certain molecules, zeotype materials can only accommodate guest molecules that have access to their pores, and they are, therefore, often referred to as molecule sieves. Conspicuously, they show unique reactant, transition state, or product shape selectivity in catalytic reactions when used as solid acidic catalysts, which is associated to confinement effects imparted by their microporosity. In many of these applications, besides acidity and shape selectivity, the mass transport rate within the pore space is a key parameter determining the overall performance.[4] These mass transfer properties are highly dependent on the mesostructure, the

[a] UNILAB, State Key Lab of Chemical Engineering, School of Chemical Engineering, East China University of Science and Technology, Shanghai 200237, P. R. China. E-mail: kakezhu@ecust.edu.cn

[b] School of Chemistry and Chemical Engineering, Henan Normal University, Xinxiang 453007, P. R. China

[c] Shanghai Research Institute of Petrochemical Technology, SINOPEC, Shanghai 201208, P. R. China

[d] Department of Chemical Engineering, University College London, London WC1E 7JE, UK. E-mail: m.coppens@ucl.ac.uk

† Electronic supplementary information (ESI) available. See DOI: 10.1039/c8cy01483c

5044 | *Catal. Sci. Technol.*, 2018, **8**, 5044–5061

This journal is © The Royal Society of Chemistry 2018

porosity and pore size distribution, as revealed by some recent diffusion measurements.[5,6] Silicoaluminophosphates (SAPOs), among other zeotype materials, find industrial applications in chemical processes, such as hydroisomerization and methanol-to-olefin conversions. In particular, SAPO-11 is well suited for hydroisomerization of *n*-paraffins, thanks to its unidimensional **AEL** structured topology with tubular and elliptically shaped pores of 4.0 × 6.5 Å that lead to high isomer selectivity.[7–9] The catalytic performance of SAPO-11 can be maximized by manipulating mesostructural features, such as crystallite size, porosity, acidity or their distribution.[10–13] Although the acidity of SAPO-11 plays a determining role in the activity of skeletal isomerization, the mesostructure of the crystallites can significantly influence the product distribution as well.[12,13]

Hydroisomerization of *n*-paraffins to branched isomers is an important process in the petroleum industry,[14] as *iso*-paraffins can improve the octane number of gasoline (C_5–C_8) and the cold-flow properties of middle-distillate fuels (C_{16}–C_{22}) and lube base oils.[15–20] Catalysts for hydroisomerization of *n*-paraffins are bifunctional, composed of noble metals (Pt, Pd, Ru, *etc.*) supported on solid acids, such as aluminosilicates, *i.e.*, zeolites (ZSM-5,[16,21,22] ZSM-22,[21,23,24] beta,[21,25–28] *etc.*), or SAPOs. C_5–C_7 alkanes dehydrogenate rapidly on noble metal centres to produce the corresponding *n*-alkenes. The latter enter the micropores, where acidic sites are situated, to undergo skeletal isomerization to *iso*-alkenes with identical numbers of carbon atoms. *Iso*-alkenes desorbing from acid sites are subsequently hydrogenated to *iso*-alkanes on metal centres before leaving the catalyst surface. Under ideal operating conditions, *n*-alkenes are in equilibrium with *n*-alkanes, because of the high (de)hydrogenation rate with respect to the isomerization rate.[29] Mono-branched isomers (MBs) and di-branched isomers (DBs) are produced sequentially, in addition to some highly branched isomers that are susceptible to β-scission, which leads to unwanted cracking side-products.[29–33] Zeolites and SAPOs possessing one-dimensional channels are the preferred acid components, because they endow the catalysts with exceptional shape-selectivity, to produce primarily MBs that are more stable towards cracking.[29,31] Cracking of DBs formed inside the micropores of **AEL** is responsible for the high cracking rate, as their bulkier size slows down diffusion out of the micropores, which prolongs the retention time and increases likelihood of cracking.[29]

Over the past decade, it has become increasingly recognized that integration of auxiliary macro- or meso-porosity into SAPO-11 crystals is an effective route to increase the isomer selectivity. By constructing SAPO-11 with a hierarchical architecture, the diffusion pathway for primary isomer products can be shortened, which minimizes subsequent cracking probability. Targeting this goal, several synthesis strategies have been reported. Ryoo *et al.*[34] have synthesized micro- and meso-structured SAPOs using multiamines with an amphiphilic structure, and the corresponding Pt/SAPO exhibited a maximum *i*-C_7 yield of 51% and enhanced catalytic activity.

Kim *et al.*[12] have generated SAPO-11 with secondary mesoporosity using amphiphilic organosilanes and carbon blacks. The organosilane templating method produced mesoporous SAPO-11 with a large amount of external acidity, while the carbon templating method produced a sample containing predominantly internal acid sites. They found that the hydroisomerization selectivity of the catalysts can be significantly enhanced by facilitating hydrocarbon diffusion *via* the formation of secondary mesopores, while suppressing the formation of external acid sites that can non-selectively catalyse consecutive cracking reactions. Xiao's group[35,36] has synthesized hierarchically porous SAPO-11 s containing an abundance of medium and strong acid sites, in the presence of polyhexamethylene biguanidine (PHMB) as a mesopore template. The corresponding hierarchical Pt/SAPO-11 zeolite exhibited a high conversion of *n*-dodecane and enhanced selectivity for branched products, as well as reduced selectivity for cracking products, compared with conventional Pt/SAPO-11 zeolite. Bao's group[13] has found that hierarchical SAPO-11 molecular sieves synthesized by using tetradecylphosphoric acid (TDPA) as template for the mesopores had a much higher mesoporous volume consisting of intracrystalline mesopores of 4–7 nm and a larger number of medium and strong Brønsted acid sites, active for *n*-octane isomerization.

These studies demonstrate that both acidity and porosity are important to increase the isomer selectivity. Up to date, the developed methods mainly rely on the use of porogens or structure directing agents to tailor additional porosity, or to hinder the growth of SAPO-11 crystals to their full size. Low crystallinity and poor control over crystal size at the mesoscale are still outstanding issues. On the one hand, a stronger acidity is preferred, as it lowers the temperature at which the overall reaction is operating in an intrinsic reaction controlled regime that benefits isomerization over cracking.[37,38] An excessive population of acidic sites on the external surface of the crystals should be avoided, so as not to produce highly branched isomers that are more susceptible to cracking. On the other hand, from a mass transfer standpoint, a small crystallite size and enhanced pore connectivity are desirable to promote mass transfer and reduce residence time for isomers.[13,20] For practical applications, a low-cost and simple preparation, as well as potential scalability are considered important criteria for an industrially feasible solution. Henceforth, more promising protocols to generate hierarchical SAPO-11, which take these factors into consideration, are required.

Crystallization history and the underlying formation mechanism can significantly influence the structure and properties of zeotype materials. Microwave assisted crystallization,[39] dry gel conversion (DGC),[40,41] ion-thermal synthesis,[42] and silica colloid precursors,[43,44] have been successfully used to tailor hierarchical zeolites. Specifically, zeolite growth *via* non-classical oriented attachment has been found to be a predominant pathway for their formation under certain circumstances. In particular, Tsapatsis *et al.*[45] have shown that silicalite-1 grows mainly through the attachment of tiny

This journal is © The Royal Society of Chemistry 2018

Catal. Sci. Technol., 2018, **8**, 5044–5061 | **5045**

particulates. Kumar et al.[46] have found that SSZ-13 crystals grown by atom-by-atom or oriented attachment crystallization pathways have distinct morphological features. In DGC growth, oriented attachment has generally been found to be the main crystallization route for several zeolitic materials, such as beta,[40,41] SAPO-34,[47] ZSM-5,[48] ZSM-11[49] and SAPO-11.[50] Intriguingly, the oriented attachment can also be tailored to construct hierarchical zeolites consisting of a super-structure of aligned nanocrystallites, thus providing a new route to generate hierarchical zeotype crystals.[41,42,51]

Recently, we have demonstrated that manipulation of the crystallization process can be a successful way to fabricate hierarchical SAPO-11. Non-classical "from-shell-to-core" growth of hierarchically organized SAPO-11 has been reported in the presence of a small molecular growth modifier (1,2,3-hexanetriol) under agitating conditions.[52] An oriented assembly strategy to construct hierarchical architectures of SAPO-11 using prefabricated nanocrystallites as precursor was also put forward in a preceding article.[51] In that work, it is demonstrated that cationic polymers or additives can lead to the formation of agglomerated architectures, whilst additives interacting weakly produce a self-assembled house-of-cards structure, made up of nanosheets. Here, we report the fabrication of house-of-cards structured SAPO-11 via an appealing, porogen-free synthesis route. Furthermore, the addition of a new and cheaper growth modifier, cellulose 2-(2-hydroxy-3-(trimethylammonium)propoxy) ethyl ether chloride (PQ-10), to expand the mesopore dimension and simultaneously reduce the lateral size of nano-sheets will also be presented. The underlying formation mechanism, including the effect of additives on selecting the morphology during crystallization, will be discussed through comparison with controlled samples. Next, the two obtained architectures in the absence and presence of PQ-10 will be inspected by using a range of characterization techniques, such as XRD, N_2 adsorption, SEM, and TEM, to illustrate their textural and acidic properties. Finally, the catalytic performance for hydroisomerization of n-heptane will be investigated and correlated with mass transfer properties revealed by kinetic and diffusivity measurements.

Experimental

Preparation of SAPO-11

The initial gel with molar ratio 1.2 DPA : 1.0 Al_2O_3 : 1.0 P_2O_5 : 0.6 SiO_2 : 50 H_2O was prepared as follows: 48.55 g pseudo-boehmite (PB, 75 wt% Al_2O_3, Aluminium Corporation of China) was hydrolyzed in 257.57 g deionized water, while stirring. 76.86 g of phosphoric acid (≥85.0 wt%, Shanghai Lingfeng Chemical Reagent Co. Ltd.) was added to the above mixture and homogenized overnight (12 h). 42.92 g of tetraethyl orthosilicate (TEOS, 28.0 wt% SiO_2, Shanghai Lingfeng Chemical Reagent Co. Ltd.) was introduced into the mixture while stirring for 2 h, followed by addition of 40.48 g of dipropylamine (DPA > 99 wt%, TCI). The mixture was homoge-

nized by stirring for an additional 5 h, before transferring to a 353 K oil bath to evaporate the water solvent. The obtained dry gel was ground into a fine powder with a mortar and pestle before crystallization. A portion of 3.00 g dry gel powder was introduced in a beaker placed in a Teflon-lined stainless steel autoclave; 10.00 g of water was poured outside the beaker as a source of steam. The autoclave was heated to 473 K for various durations in the crystallization study, and quenched with tap water after removal from the oven. The intermediates were collected for characterization.

To prepare prefabricated nanocrystallites, dry gel powder was pre-crystallized at 473 K for 2.5 h, collected and used as precursor for the synthesis of hierarchical SAPO-11 s. The obtained powder was used as precursor for subsequent preparation without further treatment or purification. In a typical synthesis of hierarchical SAPO-11, 3.00 g of SAPO-11-2.5 h was mixed with H_2O (50 mL) without porogen, and homogenized at ambient conditions for 1 h. The mixture was then transferred into a Teflon-lined stainless steel autoclave and hydrothermally crystallized at 473 K for 2 days while tumbling (50 rpm). The resultant product was washed with deionized water by centrifugation, dried at 373 K for 12 h and calcined at 823 K in a muffle oven for 10 h. The product prepared in this way was denoted as SAPO-11-T, T representing 'tumbling'. For the sake of comparison, a contrasting sample was also synthesized from the same prefabricated precursor dispersed in aqueous mixture, but without tumbling, denoted as SAPO-11-WT, WT standing for 'without tumbling'. 3.00 g of SAPO-11-2.5 h was mixed with H_2O (50 mL) without porogen, but a resumed crystallization was carried out under static conditions for 2 days at 473 K. Again, the product was washed with deionized water by centrifugation, dried at 373 K for 12 h and calcined at 823 K for 10 h.

A third hierarchical SAPO-11 sample was synthesized in an analogous manner, except that 3.00 g of SAPO-11-2.5 h was mixed with a 20.0 mL ethanolic solution of 0.36 g of Polyquaternium-10 (PQ-10, cellulose 2-(2-hydroxy-3-(trimethylammonium)propoxy) ethyl ether chloride). To rule out the effect of ethanol, the mixture was first dried by heating, before replenishing with H_2O to achieve the desired composition. Such a product was labeled as SAPO-11-PQ. PQ is an abbreviation for the modifier.

For comparison, a sample of SAPO-11 was synthesized under commonly used static conditions. The molar composition of the synthesis gel was again 1.2 DPA : 1.0 Al_2O_3 : 1.0 P_2O_5 : 0.6 SiO_2 : 50 H_2O. A typical synthesis procedure was as follows: 1.46 g of pseudoboehmite and 2.31 g of phosphoric acid were hydrolyzed in deionized water while stirring for 12 h. 1.29 g of TEOS was subsequently added to the mixture and stirred vigorously for 2 h. Then, 1.21 g of DPA was slowly added and the mixture was stirred for 8 h. The synthesis gel was hydrothermally crystallized at 473 K for 3 days under static conditions. The as-synthesized SAPO-11 was filtered, washed with deionized water, and dried at 393 K for 5 h. Thereafter, the sample was calcined at 823 K for 15 h. The

5046 | Catal. Sci. Technol., 2018, 8, 5044–5061

This journal is © The Royal Society of Chemistry 2018

obtained product was denoted as SAPO-11-C, with the suffix C standing for 'conventional'.

Catalyst preparation

The Pt/SAPO-11 catalysts were prepared by incipient wetness impregnation of SAPO-11 with an aqueous solution of H_2PtCl_6, followed by drying and calcination at 673 K for 3 h. The Pt content of each catalyst was kept at 0.5 wt% for all samples.

Characterizations

The phase structure of the SAPO-11 was characterized by powder X-ray diffraction (XRD) patterns, recorded on a Rigaku D/Max 2550 VB/PC diffractometer operating at 40 kV and 100 mA with Cu Kα (λ = 1.5418 Å) as X-ray source. The patterns were collected over a 2θ range from 3 to 50°, with a scanning speed of 8° min^{-1}. The size and morphological features of the samples were determined by means of scanning electron microscopy (SEM) images, recorded with a NOVA Nano SEM450 microscope. Transmission electron microscope (TEM) micrographs were obtained using a JEM-2011 (JEOL) electron microscope. A drop of the examined solution was placed on a TEM grid covered by a perforated carbon film. Nitrogen adsorption and desorption isotherms were measured on an ASAP 2020 (Micromeritics, USA) physisorption apparatus at 77 K, after samples were outgassed at 623 K under vacuum for 6 h. The surface areas and pore volumes were determined by the Brunauer–Emmett–Teller (BET) method, and non-local density functional theory (NLDFT) method, respectively. Micropore volumes were derived from a t-plot approach, and the total pore volume values were estimated from the adsorbed quantity at a relative pressure P/P_0 = 0.99. Mercury intrusion tests were performed by using an AutoPore IV 9500 Micrometrics instrument. The intrusion volumes were measured at stepwise increasing pressures, equilibrated at each pressure step. The intrusion measurements started from vacuum conditions, and the extrusion measurements terminated at normal pressure. The pore size distribution was calculated according to the intrusion curves. A Micromeritics Autochem 2920 was used for chemisorption measurements. The exposed active surface areas of the catalysts were determined via H_2 titration at room temperature. In each experiment, 0.10 g of catalyst was used. The catalyst was heated to 673 K in 10% H_2/Ar with a flow rate of 30.0 mL min^{-1}, ramped up at a rate of 5 K min^{-1} and kept at 673 K for 3 h. After reduction, the catalyst was purged with an ultra-high-purity helium flow, before being cooled to room temperature. H_2 pulses were introduced over the reduced catalyst, and the H_2 uptake for each pulse was monitored using a thermal conductivity detector (TCD). Elementary composition was measured by inductively coupled plasma optical emission spectrometry (ICP-AES) on an IRIS 1000 instrument. The acidity of SAPO-11 was probed by alkaline molecules (pyridine, Py, or 2,4,6-collidine, Coll) desorption infrared (Py-IR, Coll-IR) spectra on a Spectrum 100 FT-IR spectrometer

(Nicolet Co., USA). All samples were pressed into self-supporting wafers (diameter: 1.4 cm, weight: 166 mg) and were pre-heated at 723 K for 4 h under vacuum (1.3 × 10^{-2} Pa). The background baselines of the samples were collected and subtracted at room temperature. The amount of adsorbed probe molecules was calculated from the integrated area of given bands with their distinct molar extinction coefficients ($\varepsilon_{H\text{-bond}}$(1638 cm^{-1}) = 1.9 cm μmol^{-1},[53] $\varepsilon_{Brønsted}$(1545 cm^{-1}) = 1.67 cm μmol^{-1} and ε_{Lewis}(1455 cm^{-1}) = 2.22 cm μmol^{-1}).[54] The diffusivity of 2-methylhexane in the SAPO-11 samples was measured by an IGA Intelligent Gravimetric Analyzer (IGA-100), which can acquire isotherms and the corresponding kinetics of adsorption and desorption. The system consists of a fully computerized microbalance, which automatically measures the weight of the sample sorbents as a function of time with the gas vapor pressure and sample temperature under computer control. The balance and pressure control system were isothermal to ±0.01 K, to eliminate changes due to variation in the external environment. The microbalance had a long-term stability of ±1 μg with a weighing resolution of ±0.2 μg. The sample (100 ± 1 mg) was outgassed until constant weight, at a pressure of <10^{-6} Pa at 573 K. When the samples were cooled down to 365 K, the temperature was set to the reaction temperature, and isotherms and the corresponding kinetics of adsorption and desorption were determined at a set pressure or partial pressure steps.

Catalytic activity assessments

The hydroisomerization of n-heptane was carried out in a quartz glass fixed-bed, continuous flow reactor at atmospheric pressure. The catalyst loading was 1.2 g (40–60 mesh). Prior to reaction, the catalyst was reduced in H_2 flow (23 mL min^{-1}) at 673 K for 3 h, then cooled down to the reaction temperature under H_2 flow. n-Heptane was introduced to the reactor using a constant-flux pump, which gave a H_2/n-heptane molar ratio of 5. The weight hourly space velocity (WHSV) of n-heptane was 1.0 g$_{n\text{-heptane}}$ (g$_{cat}$ h)$^{-1}$. The product gas mixture was analyzed periodically with an on-line gas chromatograph equipped with a flame ionization detector (FID) and a HP-PONA capillary column (50 m × 0.2 mm × 0.5 μm). The oven temperature was kept at 343 K.
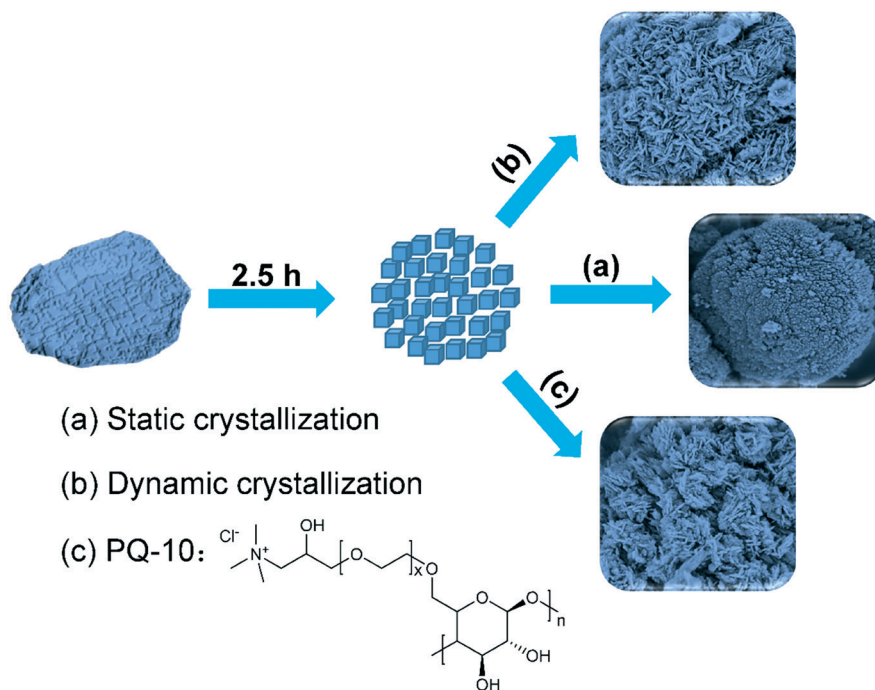
Kinetic experiments

A catalyst with a mass of 0.025 g to 0.15 g (40–60 mesh) was diluted in the fixed-bed reactor with the same mass of quartz sand, n-heptane was introduced into the reactor by a constant-flux pump. The gas flow was varied between 23 and 92 mL min^{-1}. The n-heptane to H_2 ratio was kept at 1 : 26 during kinetic studies. The n-heptane consumption rates were measured at temperatures between 523 K and 653 K, and the conversion was kept below 10% for the measurements.

Results and discussion

Synthesis of hierarchical SAPO-11

In a preceding article, we have shown that crystallization of SAPO-11 during DGC synthesis proceeds predominantly through the non-classical oriented attachment crystallization pathway.[51] DGC favours oriented attachment growth because the concentration of ingredients is high, leading to a fast nucleation rate as a result of a high supersaturation ratio, which favours synthesis of nanocrystallites with narrow size distribution.[50,55,56] The apparent lack of liquid water may also restrict atom-by-atom growth in a LaMer mechanism,[57] as the formation of soluble molecular species is a prerequisite for such classic crystallization. In the same publication, it was demonstrated that the crystallization process may be interrupted at an early stage to purposefully produce nanocrystallites, whose sizes span from 15 to 30 nm (Scheme 1a). The use of such nanocrystallites as building blocks to construct a hierarchical architecture, assisted by porogens, has been reported in our previous work.[51] In the present article, the use of these nanocrystallites to prepare hierarchical SAPO-11 through crystallization control in the absence of porogen is explored.

In a porogen-free synthesis, the nanocrystallites were collected by separation *via* centrifugation, and re-dispersed in H_2O to achieve a crystallites-to-H_2O mass ratio of $3:50$ (Scheme 1b). Secondary crystallization was carried out under tumbling at 473 K for 48 h. The dilution of these prefabricated nanocrystallites reduces the supersaturation ratio of the system, in order that no more nucleation will occur when crystallization is resumed. In addition, the pH for the

dispersion was found to be close to 7.5 (measured by pH meter), which approaches neutral conditions that disfavours dissolution of prefabricated nanocrystallites. Such crystallization condition control is believed to facilitate the nonclassical oriented attachment growth of crystalline building blocks, and can minimize Ostwald ripening or the atom-by-atom growth pathway. Excessive dilution should be avoided, so that the concentration of nanocrystallites is sufficiently high to favour collision,[56] since collision is a prerequisite for attachment growth. Tumbling is necessary, as the size of these nanocrystallites exceeds the size (normally <10 nm) of inorganic building blocks that are suitable to be used directly for self-assembly.

In a second synthesis route, the growth modifier, PQ-10, was chosen as a pore expander and was introduced into the synthesis mixture before the secondary crystallization process (Scheme 1c), with the aim to create more open auxiliary porosity that has been regarded as a crucial structural factor to enhance mass transfer.[58,59] PQ-10 has more C–OH functional groups and only one positively charged centre. C–OH groups have been disclosed to inhibit the growth of SAPOs by enclosing their external surfaces.[47,52] Cationic porogens with high charge density often cause flocculation-like agglomeration of primary building blocks, in which preferential orientation during the alignment of nuclei is lost.[46] Porogens containing C–OH groups tend to direct the formation of a high-order superstructure, owing to crystallographic alignment with preferential orientation.[60] PQ-10 with a low charge density and more C–OH groups has never before been employed as porogen for the fabrication of hierarchical SAPOs. The yields for SAPO-11-C, SAPO-11-T and SAPO-11-PQ

Scheme 1 Proposed formation of SAPO-11 in DGC synthesis (a) and the synthetic strategies for the oriented assembly of prefabricated nanocrystallites with growth modifiers, without growth inhibitors (b), or with PQ-10 (c), to construct diversified architectures.

in the above preparation are 96%, 93% and 91%, respectively, suggesting an efficient synthesis of hierarchical SAPO-11 s using orientated assembly approach with respect to standard hydrothermal synthesis.

XRD characterization

In Fig. 1, the XRD patterns for the hierarchical samples are juxtaposed with those of a standard SAPO-11-C for comparison. All diffraction peaks for SAPO-11-T and SAPO-11-PQ match the simulated powder diffraction pattern for the typical SAPO with **AEL** topology (JCPDS no. 42-0428),[61,62] and no impurities or unconverted amorphous phase can be identified. The intensity of the reflection lines for SAPO-11-T and SAPO-11-PQ is comparable to the standard SAPO-11-C, showing that the adoption of the tumbling process or inclusion of growth modifiers does not affect the integrity of the intrinsic framework. Relative crystallinity of 94% and 83% for SAPO-11-T and SAPO-11-PQ can be inferred by setting SAPO-11-C as 100%. The preservation of a high degree of crystallinity for SAPO-11-T and SAPO-11-PQ samples can be ascribed to the precrystallization process, which has produced nano-crystallites with an occluded structure directing agent DPA that protects the structure by a templating effect in the subsequent crystallization process.

SEM and TEM characterizations

SEM and TEM micrographs were collected to disclose the microscopic structure of the calcined samples, as displayed in Fig. 2. A panoramic image in Fig. 2a for SAPO-11-T discloses that the sample consists of agglomerates of uniform particulates between 2 and 3 μm. Images of higher magnifications (Fig. 2c and e) show that the particulates are made up of nano-sheets with an average thickness of 20 to 40 nm, and the lateral size of the nano-sheets ranges from 150 to 300 nm. The surface of these nano-sheets has a rough appearance, as a consequence of fused building blocks of 20 to 40 nm, a size that is close to the nanocrystallites that have been collected after the initial DGC process (Fig. S1†), implying an oriented attachment growth history. SAPO-11-T was
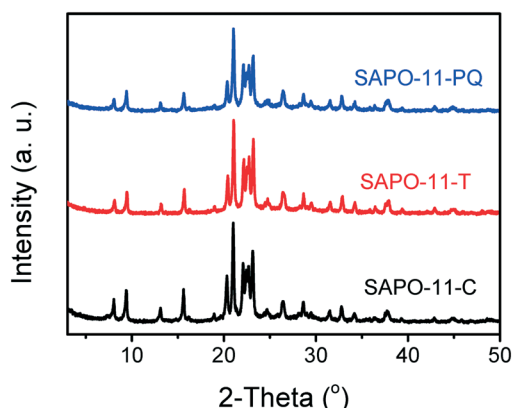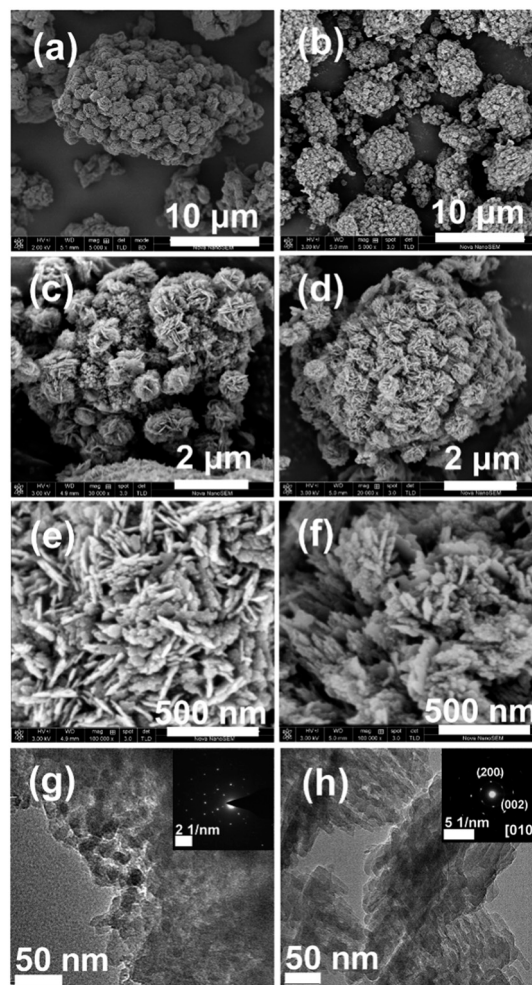

Fig. 2 SEM (a, c and e), TEM (g) images and associated SAED (inset of g) pattern of SAPO-11-T; SEM (b, d and f), TEM (h) images and associated SAED (inset of h) pattern of SAPO-11-PQ.

sonicated to prepare a detached piece for transmission electron microscopy (TEM) measurement. The TEM images for SAPO-11-T reveal that the individual nano-sheets have a lateral size of approximately 100 to 200 nm, made up of primary particles ranging from 20 to 40 nm, as shown in Fig. 2g, which confirms SEM observations. The corresponding selected area electron diffraction (SAED) pattern (inset of Fig. 2g) consists of spots that are characteristic of single crystals. The building blocks of the nanocrystallites are aligned along the same crystallographic axis, which is a typical feature of a mesocrystal, as summarized by Cölfen et al.[63] Parts of the building blocks or particulates are found to have fused into adjoining ones, which can be attributed to the elimination of grain boundaries, which lowers the interfacial energy of the system.

For SAPO-11-PQ, the inclusion of growth modifier PQ-10 contributes to the reduction of the nano-sheet size and improvement of homogeneity, as demonstrated by the low-magnification image shown in Fig. 2b. An average particulate size from 0.6 to 2 μm can be identified, with a mean size of 1

Fig. 1 XRD patterns of SAPO-11-C, SAPO-11-T and SAPO-11-PQ.

This journal is © The Royal Society of Chemistry 2018

Catal. Sci. Technol., 2018, 8, 5044–5061 | 5049

μm. Importantly, the house-of-cards architecture is more ordered and open to the exterior. The lateral size of the nano-sheets is found to range from 50 to 200 nm, with an average reduced lateral size of approximately 100 nm (Fig. 2d and f), suggesting a hindering effect for crystal growth *via* attachment imposed by the presence of PQ-10, which serves as growth modifier. Moreover, the surface of the nano-sheets is corrugated and disrupted by mesoporous regions with respect to SAPO-11-T. Fig. 2h shows a TEM image of the synthesized SAPO-11-PQ, which reveals that a sheet consists of fused particles with voids in between. Between the dark, sheet-like particles, bright areas indicate the presence of a large number of mesopores. The lateral size of dark areas for primary building blocks is *ca.* 20–40 nm. These microscopic structural features agree well with the corrugated surface in SEM images. The selected area electron diffraction (SAED) patterns (inset of Fig. 2g and h) of the SAPO-11-PQ shows that the sample contains large crystalline domains, with the normal of the sheets running parallel to the [010] direction. It is noteworthy that the unidimensional micropores for the **AEL** topology run along the [100] axis. Hence, the presence of mesopores traversing the sheet is important for mass transfer, as mesopores reduce the diffusion pathway. In clear contrast, the SAPO-11-C consists of micron-sized crystals with rough surfaces in addition to detached smaller ones, which is in line with previous reports (Fig. S2†).[51] In brief, the growth modifier assists the oriented assembly of nano-crystallites towards building up a more open architecture that can be accessed easily from the external surface. Furthermore, the modifier, PQ-10, is also crucial to reduce the crystallite size while retaining a sheet-like morphology.

N₂ physisorption and mercury intrusion measurements

N_2 physisorption measurements were carried out at 77 K and were used to deduce the textural properties of the hierarchical samples, as compiled in Fig. 3a and Table 1. The N_2 adsorption–desorption isotherms for SAPO-11-C can be classified as type I, from which the micropore-filling at low relative pressures ($10^{-6} < P/P_0 < 0.01$) can be clearly observed. In addition, uptake of N_2 at P/P_0 close to 1.0 is ascribed to capillary effects due to the presence of large voids as a result of aggregation of zeolitic particulates.[12] It is notable that the SAPO-11-T (189 m² g⁻¹) and SAPO-11-PQ (239 m² g⁻¹) samples have a much larger BET surface area than SAPO-11-C (134 m² g⁻¹), with a major contribution from the external surface area. The difference between the two samples shows the effect of PQ-10 over the pore structure. In addition to the micropore-filling process, SAPO-11-T and SAPO-11-PQ samples exhibit a more pronounced N_2 uptake than SAPO-11-C in the P/P_0 range of 0.8–1.0. Therefore, isotherms for SAPO-11-T and SAPO-11-PQ can be categorized as a hybrid of type I and type IV that is often found for hierarchical SAPO-11.[12,20,35,64] The values for the micropore volume, inferred from the *t*-plot method, are 0.05, 0.05 and 0.06 cm³ g⁻¹ for SAPO-11-C, SAPO-11-T and SAPO-11-PQ, respectively. The retained micropore
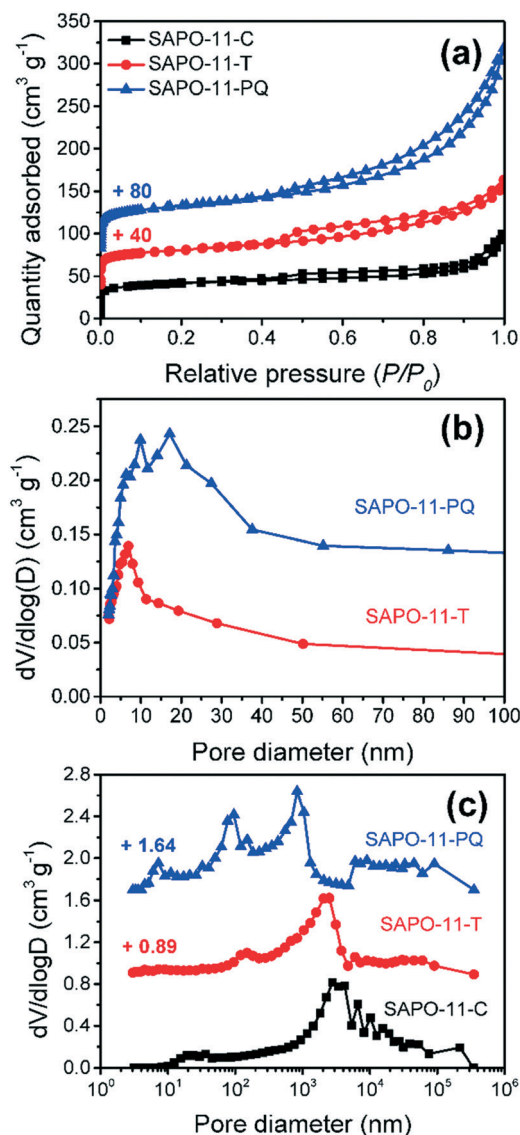

Fig. 3 N₂ adsorption/desorption isotherms of all samples (a) and the corresponding pore size distribution for all samples (b). Mercury intrusion based pore size distribution of SAPO-11-C, SAPO-11-T and SAPO-11-PQ (c).

volume for hierarchical samples is consistent with the high crystallinity for the samples, meaning that introduction of auxiliary porosity in this way does not affect the inherent microporosity. The mesopore volume inferred by subtracting the micropore volume from the total pore volume for SAPO-11-C is 0.13 cm³ g⁻¹, whereas SAPO-11-T (0.16 cm³ g⁻¹) and SAPO-11-PQ (0.29 cm³ g⁻¹) have a much larger mesopore volume. A conspicuous hysteresis loop can be detected for SAPO-11-PQ, in line with a larger mesopore volume, implying that PQ-10 hinders the fusion of primary crystallites and enlarges the space between them. The corresponding pore size distribution for the hierarchical samples is exhibited in Fig. 3b: SAPO-11-T and SAPO-11-PQ show broad pore size distributions ranging from 5 to 40 nm. For SAPO-11-PQ, the mean mesopore size is around 20 nm, which is much larger

5050 | *Catal. Sci. Technol.*, 2018, **8**, 5044–5061

This journal is © The Royal Society of Chemistry 2018

Table 1 Textural properties of SAPO-11-C, SAPO-11-T and SAPO-11-PQ derived from N_2 physisorption isotherms, the Pt dispersion on the supported catalysts, and the molar composition of the samples

Sample	$S_{BET}{}^a$ (m^2 g^{-1})	$S_{micro}{}^b$ (m^2 g^{-1})	V_{total} (cm^3 g^{-1})	$V_{micro}{}^b$ (cm^3 g^{-1})	$V_{Hg,total}{}^c$ (cm^3 g^{-1})	Pt dispersion^d (%)	Molar composition^e
SAPO-11-C	134	91	0.18	0.05	0.84	48.9	$Al_{0.85}Si_{0.11}P_{0.68}O_{0.90}$
SAPO-11-T	189	102	0.21	0.05	1.17	63.8	$Al_{0.74}Si_{0.10}P_{0.58}O_{0.73}$
SAPO-11-PQ	239	125	0.35	0.06	1.40	68.7	$Al_{0.78}Si_{0.11}P_{0.61}O_{0.82}$

^{a} Calculated by the BET method in the P/P_0 range of 0.05–0.25. ^{b} Calculated using the t-plot method. ^{c} Measured by mercury intrusion. ^{d} Pt determined by H_2 pulse chemisorption after depositing 0.5 wt% Pt. ^{e} Determined by ICP-AES.

than the one generated by using organosilanes, which lies between 2 and 4 nm.[12] For all samples, a forced closure of the desorption branch at a relative pressure of *ca.* $P/P_0 = 0.45$ is observed, indicating that there are small amounts of constricted mesopores in these materials.[65] Complementary mercury intrusion experiments were carried out to detect the existence of macropores that are beyond the detection limit of N_2 physisorption.[66] The obtained pore size distributions are plotted in Fig. 3c for SAPO-11-C, SAPO-11-T and SAPO-11-PQ, respectively. Macropores larger than 1 μm are attributed to the presence of interparticle space. For SAPO-11-C, the median macropore size appears at *ca.* 3 μm, in addition to a broad range of wider pores. On the other hand, the mercury intrusion measurements show that SAPO-11-T possesses two major types of macropores, with median pore size centred at *ca.* 2 μm and ~150 nm. The former is attributed to the pores between organized crystals, while the latter belongs to macropores created between nano-sheet building blocks. The SAPO-11-PQ includes three types of pores, with mean pore sizes centred at *ca.* 0.83 μm, 95 nm and 7 nm, which can be attributed to interparticulate space, voids between nanosheets and mesopores that are accessible from external surfaces, respectively. Textural property measurements clearly show the hierarchical porous nature of SAPO-11-T and SAPO-11-PQ, in which the latter is comprised of both meso- (2–50 nm) and macro- (>50 nm) pores. The pore volumes inferred from mercury porosimetry increase in the order SAPO-11-C (0.84 cm^3 g^{-1}) < SAPO-11-T (1.17 cm^3 g^{-1}) < SAPO-11-PQ (1.40 cm^3 g^{-1}), representing macro- and meso-pore volumes that can be accessed from the external surface with pore diameters above 4 nm.[59]

Formation mechanism and advantage of the preparation

So far, the successful porogen-free synthesis of hierarchical SAPO-11-T, featuring a two-dimensionally assembled architecture has been demonstrated. This synthesis method forms sheet-like particles, assembled into a house-of-cards architecture, as illustrated in Scheme 1b. It is proposed that this is due to growth by attachment of nanocrystallites during the secondary crystallization process while tumbling the suspension. In SAPO-11-T synthesis, the presence of occluded DPA in the micropores and a concurrent low pH may stabilize nanocrystalline nano-building blocks and limit their dissolution, and, thereby, minimize Ostwald ripening. Indeed, no substantial dissolution of nanocrystallites was identified by

detecting the inorganic contents of the mother liquor after the crystallization process, as only several ppm of Al or P were determined by using ICP-AES. The limited dissolution also excludes classical atom-by-atom growth along the crystal surfaces as an important contributor. Meanwhile, a sufficiently high concentration of prefabricated nanocrystallites under tumbling crystallization conditions promotes their collision, which is a prerequisite for oriented attachment growth to predominate. For the sake of comparison, another sample was crystallized under static conditions from the same prefabricated nanocrystallites, which is labeled as SAPO-11-WT. Although the XRD peak positions (Fig. S3a†) correspond again to an **AEL** topology, the SEM images (Fig. S3b and c†) show that the sample has lost the house-of-cards feature of assembled nanosheets, presumably owing to the quick precipitation of nanocrystallites, as a result of their low surface-to-volume ratio. From this, it is seen that tumbling is indispensable for a morphology-controlled preparation.

As for oriented alignment, **AEL** crystals have a strong propensity to align along their [010] axis,[67] which helps to understand why a sheet-like morphology is the preferred shape. The crystallographic alignment along the [010] vector to afford nano-sheets is found for additive-free systems, showing that the habitual alignment is unaffected by additives. The alignment of prefabricated nanocrystallites is, therefore, supposed to occur when neighbouring ones approach each other as a result of interparticle attraction, which imposes orientation preference in attachment growth. When the growth modifiers interact weakly with the nanocrystallites, using sucrose fatty acid esters and tris(hydroxymethyl)methyl aminomethane, their presence has no observable influence on the nano-sheets or the assembled house-of-cards architecture.[51] This may suggest that interparticle attraction still governs the oriented attachment process, and alignment takes place before fusion of the nanocrystallites. In striking contrast, for cationic growth modifiers with a high charge density, such as poly(diallyldimethylammonium chloride) and 1-ethyl-1-methylpyrrolidinium bromide, which interact strongly *via* Coulomb attraction with nanocrystallites, a quick flocculation-like agglomeration may have occurred before oriented attachment, resulting in the formation of fused nanocrystallites instead of crystallographically aligned nanosheets.[51] Hence, it can be surmised that quick agglomeration instead of oriented growth, determines the morphology when strong Coulomb attraction between additives and nanocrystallites or gravity (in the absence of tumbling)

This journal is © The Royal Society of Chemistry 2018

Catal. Sci. Technol., 2018, **8**, 5044–5061 | **5051**

overshadows interparticle interaction. These studies show that morphology selective crystallization of SAPO-11 may be modulated by the type of additive used. As assembly of nanoscopic building units is a ubiquitous phenomenon for crystalline zeotype materials,[68,69] it can be envisaged that this modulation method could potentially be extended to other zeotype materials.

From a practical viewpoint, porogen-free synthesis is an inexpensive and simple preparation method, which opens up new possibilities to control the hierarchical architecture of SAPOs by controlling the crystallization process. On the other hand, the obtained sample of SAPO-11-T has a low surface area and large crystal size, resulting from fusion of crystallites. The orientation of the sheets does not run along the channel direction. Adding a growth modifier, PQ-10, reduces the crystallites' lateral size, expands mesoporosity and enlarges the surface area (Scheme 1c). This modification makes up for the shortcomings of porogen-free synthesis. Demetallation is also known as an inexpensive method to generate hierarchical SAPOs, and can be a suitable way for certain topologies and compositions,[70] but the process can alter the composition of the parent framework, causing partial amorphization of the surface and deterioration of the acidity. Compared to known templating methods, such as soft-templating,[34] hard-templating,[12] or dual-functional structure directing agent methods,[71,72] the advantages of the current synthesis can be summarized as: low-cost synthesis, high crystallinity, small crystal size and tunable hierarchical order of the final product.

^{27}Al, ^{31}P and ^{29}Si MAS NMR characterizations

Solid state MAS NMR offers an effective technique to investigate the chemical environment of elements incorporated in the framework of SAPOs. The ^{27}Al, ^{31}P and ^{29}Si MAS NMR spectra for SAPO-11-C, SAPO-11-T and SAPO-11-PQ are shown in Fig. 4. In ^{27}Al MAS NMR spectra (Fig. 4a, d and g), the strong peaks at 39 ppm and 30 ppm present for both samples can be assigned to tetrahedrally coordinated framework aluminium atoms.[73,74] Octahedrally coordinated aluminium atoms appearing at −14 ppm were formed by an additional coordination of two water molecules to tetrahedrally coordinated aluminium atoms (Fig. 4a, d and g) and the weak signal at 8 ppm indicates the presence of a small amount of pentacoordinated aluminium atoms formed by coordination of one water molecule to tetrahedrally coordinated aluminium species (Fig. 4a).[73–75] The ^{31}P MAS NMR spectra display a strong peak at −30 ppm, assigned to tetrahedrally coordinated P in the framework. Meanwhile, the significantly weaker signal at −26 ppm was attributed to P that is additionally coordinated to y water molecules (P(OAl)$_x$(H$_2$O)$_y$ with x = 4)[75,76] or which is coordinated to y water molecules instead

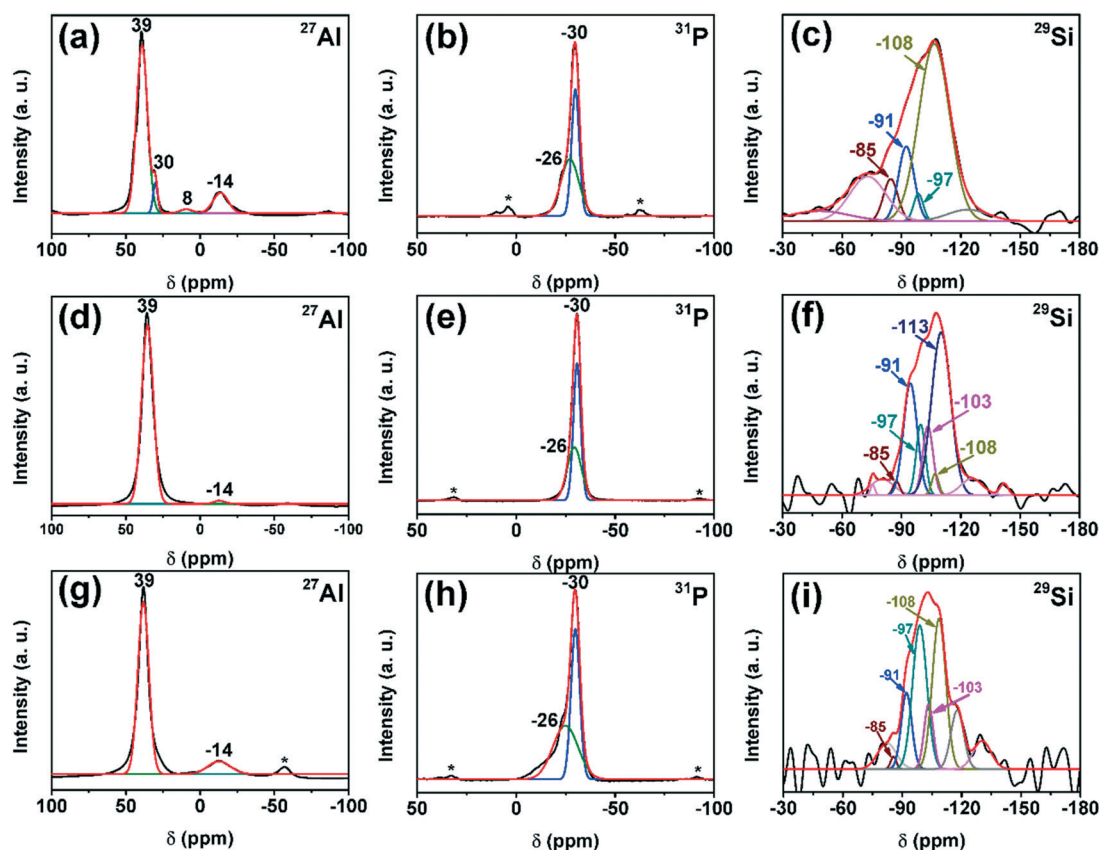Fig. 4 ^{27}Al, ^{31}P and ^{29}Si MAS-NMR spectra of calcined samples: (a, b and c) SAPO-11-C, (d, e and f) SAPO-11-T and (g, h and i) SAPO-11-PQ.

of aluminium atoms $(P(OAl)_x(H_2O)_y$ with $x = 4 - y)$ (-Fig. 4b, e and h).[75,77] The measurements indicate that SAPO-11-T and SAPO-11-PQ possess fully condensed crystalline frameworks, the same as SAPO-11-C derived from standard synthesis; no extra-framework Al or P species were detected.

The manner and content of Si incorporation into the framework governs the acid properties, such as type, strength and density, and the latter are crucial to catalytic performance. In the ^{29}Si MAS NMR spectra (Fig. 4c, f and i), all samples exhibit a broad band in the range of −80 to −120 ppm. A low signal to noise ratio in ^{29}Si MAS NMR was observed, because of the ultra long spin–lattice relaxation time (8–11 min) that challenges its further increase. The resonance peaks at −91 ppm, −97 ppm, −103 ppm, −108 ppm and −113 ppm correspond to the Si(0Si, 4Al), Si(1Si, 3Al), Si(2Si, 2Al), Si(3Si, 1Al) and Si(4Si, 0Al) environments, respectively.[78] The −85 ppm signal was attributed to $(AlO)_3Si(OH)$ or $(SiO)(AlO)Si(OH)_2$ sites rich in silanol groups.[79] The experimentally determined ^{29}Si MAS NMR spectra of all samples were simulated by using Gaussian curves, and the quantitative analysis results are shown in Table 2. It can be seen that the number of $(AlO)_3Si(OH)$ or $(SiO)(AlO)Si(OH)_2$ sites of SAPO-11-C (8.1%) is higher than that of the other two samples, showing that, whether PQ-10 is added or not during the second dynamic crystallization step, leads to less surface defective sites. For SAPO molecular sieves, when Si substitutes for P, and is incorporated into the otherwise electroneutral framework, a proton site charge balancing the framework is generated. The Si distribution into the AlPO-11 framework follows two different mechanisms:[75,80,81] the first mechanism is SM2, in which one Si atom substitutes for one P atom, producing a Si(4Al) site, which gives rise to a weak acid site. The second mechanism is SM3, in which two Si atoms simultaneously substitute for one P atom and one Al atom, leading to the appearance of Si islands with a minimum size of five Si atoms, immersed into the aluminophosphate network. The concentration of weakly acidic Si(4Al) sites is comparable for SAPO-11-T (18.7%) and SAPO-11-PQ (19.1%), which is more than for SAPO-11-C (15.6%). If some Si atoms are introduced by the substitution of two Si atoms for one P and one Al atom to form the Si domains, in addition to the SAPO region with Si(4Al), Si(nAl, 4-nSi) sites with n = 1–3, will be formed on the border of the Si domains.[82,83] The quantitative analysis confirms that the SAPO-11-PQ can improve Si dispersion to generate more Si(nAl, 4-nSi) with n = 1–3, increasing the numbers of Brønsted acid sites in SAPO-11 as a result of small Si is-

land formation, as no Si(4Si, 0Al) site are detected. In contrast, SAPO-11-T contains more Si(4Si, 0Al) sites. In brief, the ^{29}Si MAS NMR shows that the prepared hierarchical SAPO-11 can improve Si dispersion and form small Si patches, while the introduction of a hierarchical structure by the assembly of prefabricated particulates does not significantly change the structural integrity or the manner of Si incorporation. More often than not, when auxiliary porosity is integrated into the parent structure of SAPOs, the Si environment and associated acidity is altered. The oriented assembly protocol can maintain the pristine characteristic of AEL topology and Si incorporation by a stepwise crystallization, which is also a remarkable advantage of the proposed synthesis method.

Py-IR and 2,4,6-collidine-IR characterizations

The acidity is a key factor determining the intrinsic catalytic activity of zeotype materials. To probe the acidity of these materials, FTIR spectra were recorded after adsorbing the basic probe molecule pyridine (Py-IR). The patterns are displayed in Fig. 5. The bands located at 1545 cm^{-1} and 1455 cm^{-1} after pyridine adsorption can be assigned to pyridine adsorbed on Brønsted (B) and Lewis (L) acid sites, respectively.[84,85] The peak at 1490 cm^{-1} is a synergetic result from both L and B acid sites.[14] The areas of the peaks decrease gradually when raising the outgassing temperature from 473 K to 623 K, as a consequence of desorption of weakly adsorbed pyridine at elevated temperatures. Table 3 presents a quantitative overview of the acidity of the different samples on the basis of Py-IR spectra. The total number of acid sites measured at 473 K of SAPO-11-PQ (190 μmol Py g^{-1}) is greater than that of SAPO-11-C (127 μmol Py g^{-1}) and of SAPO-11-T (127 μmol Py g^{-1}) at 473 K. The number of B acid sites measured at 473 K for SAPO-11-PQ is 93 μmol Py g^{-1}, which is higher than that of SAPO-11-C (87 μmol Py g^{-1}) and SAPO-11-T (77 μmol Py g^{-1}). As strong acid sites are important for acid driven catalysis, quantitative measurements are deduced from Py-IR conducted at 623 K after desorption of weakly bound Py. The large number of B sites is tentatively attributed to the tumbling effect in crystallization, which could have enhanced dispersion of Si in the framework, as discussed earlier. The number of strong B acid sites measured at 623 K for SAPO-11-PQ is 56 μmol Py g^{-1}, which is slightly less than that of counterparts SAPO-11-C (63 μmol Py g^{-1}) and SAPO-11-T (61 μmol Py g^{-1}). Consistent with NMR data, these results clearly indicate that SAPO-11-T and SAPO-

Table 2 Deconvolution results of the ^{29}Si MAS NMR spectra of SAPO-11-C, SAPO-11-T and SAPO-11-PQ based on the normalized peak areas of the different Si species

Sample	Si(OH) or Si(OH)$_2$[a] (%) −85 ppm	Si(4Al) (%) −91 ppm	Si(3Al) (%) −97 ppm	Si(2Al) (%) −103 ppm	Si(1Al) (%) −108 ppm	Si(0Al) (%) −113 ppm
SAPO-11-C	8.1	15.6	3.6	0	72.7	0
SAPO-11-T	2.1	18.7	18.1	16.2	13.1	31.8
SAPO-11-PQ	2.2	19.1	30.1	17.2	31.4	0

[a] $(AlO)_3Si(OH)$ or $(SiO)(AlO)Si(OH)^2$ structures.

This journal is © The Royal Society of Chemistry 2018

Catal. Sci. Technol., 2018, **8**, 5044–5061 | 5053

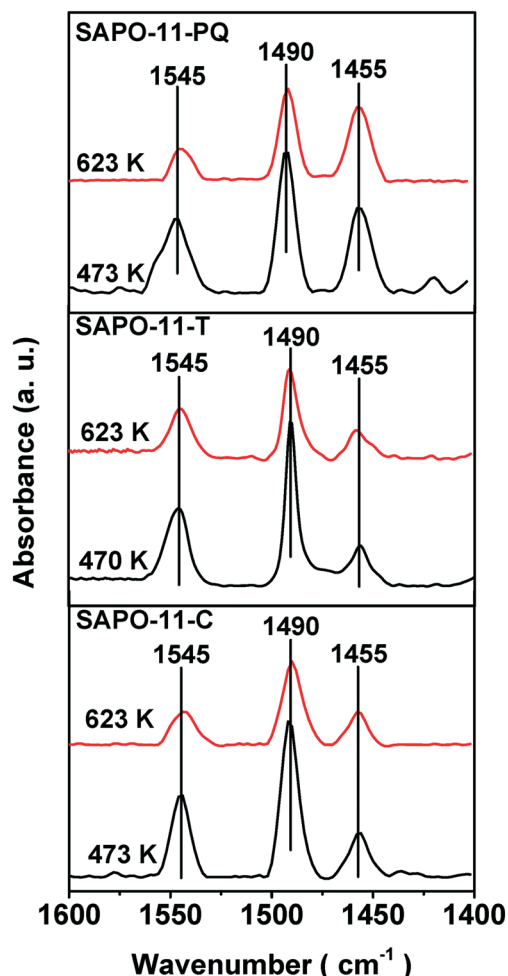**Fig. 5** FT-IR spectra of pyridine (Py) adsorbed on synthesized SAPO-11-C, SAPO-11-T and SAPO-11-PQ at 473 and 623 K, respectively.
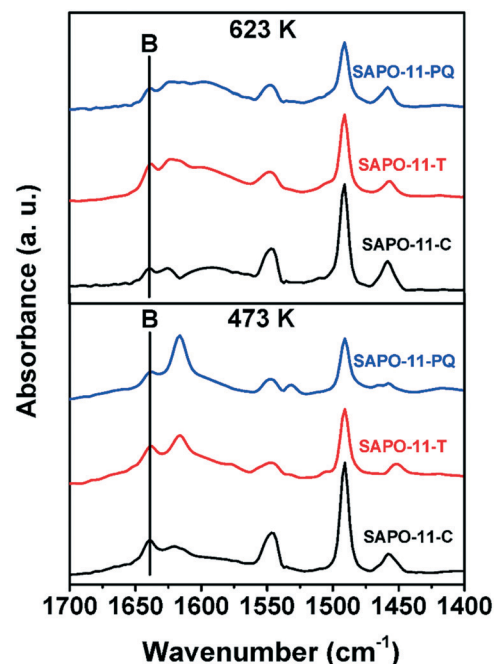

Fig. 6 FT-IR spectra of 2,4,6-collidine adsorbed on synthesized SAPO-11-C, SAPO-11-T and SAPO-11-PQ at different evacuation temperatures 473 K and 623 K. The 'B' peaks were used to quantify the amounts of Brønsted (B) acid sites.

11-PQ hold a comparable density of strong B acid sites to standard SAPO-11-C. Strong B acid sites play a determining role in the catalytic properties, as they relate to intrinsic catalytic activity.[29,33]

The accessibility of the acid sites is believed to be important for the catalytic hydroisomerization behaviour, as an excessive number of acid sites over the external surface can compromise the isomer selectivity.[12] The accessibility was investigated via 2,4,6-collidine adsorption IR spectroscopy, in a

way analogous to what has been proposed by Gilson et al.,[86] as illustrated in Fig. 6, with the quantitative data tabulated in Table 2. The kinetic diameter of 2,4,6-collidine is 7.4 Å, so that it can only be adsorbed on acid sites positioned on the external surface.[53] The band at 1638 cm^{-1} can be assigned to the adsorption of 2,4,6-collidine on B acid sites.[86,87] Therefore, the total number of strong B acid sites on the external surface can be calculated from 2,4,6-collidine-IR measurements at 623 K. The derived overall numbers of B sites are 21, 27 and 28 μmol Py g^{-1}, for SAPO-11-PQ, SAPO-11-T and SAPO-11-C, respectively. Accessibility, χ, is defined as the percentage of the number of external B acid sites to that of the total B acid sites. At 623 K, SAPO-11-T and SAPO-11-PQ showed χ values of 44.3% and 37.5%, respectively, which were much lower than that of SAPO-11-C (60.9%). This result indicates that the new synthesis method leads to the formation of a smaller amount of external B acid sites.

Table 3 Py-IR and 2,4,6-collidine-IR measurements of acidity for SAPO-11-C, SAPO-11-T and SAPO-11-PQ derived from different routes

| | Acidity amount (μmol g^{-1}) | | | | | | | |
| | Brønsted acidity[a] (1545 cm^{-1}) | | Lewis acidity[a] (1455 cm^{-1}) | | External Brønsted acidity[b] (1638 cm^{-1}) | | χ^c (%) | |
Sample	473 K	623 K	473 K	623 K	473 K	623 K	473 K	623 K
SAPO-11-C	87	63	40	28	40	28	46.0	60.9
SAPO-11-T	77	61	50	49	38	27	49.4	44.3
SAPO-11-PQ	93	56	97	91	30	21	32.3	37.5

[a] The number of Brønsted acid sites and Lewis acid sites were calculated from the Py-IR band area located at 1545 cm^{-1} and 1455 cm^{-1}, respectively. [b] The number of external Brønsted acid sites was calculated from the 2,4,6-collidine-IR band area located 1638 cm^{-1}. [c] Accessibility, χ, was defined as the ratio of the number of external Brønsted acid sites to that of total Brønsted acid sites.

5054 | Catal. Sci. Technol., 2018, 8, 5044–5061

This journal is © The Royal Society of Chemistry 2018

n-Heptane hydroisomerization using the Pt/SAPO-11 catalysts

Catalytic properties of the hierarchical and standard samples were assessed after loading of Pt as (de)hydrogenation component to form bifunctional catalysts. The loading was kept above 0.5 wt%, because, above this value, concentration of adsorbed species on the metal centres reaches equilibrium; therefore, the catalytic performance is solely dependent on the properties of the acidic component of the catalyst.[29,30] The dispersion for Pt, determined by H_2 titration, was found to increase from 48.9 on a SAPO-11-C support, to 63.8 and 68.7 on SAPO-11-T and SAPO-11-PQ (Table 1), respectively. This trend follows the same one as the surface area variation among samples, suggesting that the hierarchical architecture tends to promote metal dispersion. The catalytic assessments were carried out at temperatures ranging from 473 to 693 K. Fig. 7a shows the conversion vs. temperature for n-heptane hydroisomerization. The onset temperature for n-heptane conversion emerges at almost the same temperature of ca. 473 K for the three samples, suggesting that they have close acid strength, according to the universal Brønsted relationship in acid driven catalysis. This observation is consistent with Py-IR data that the samples have identical acid strength

and a comparable amount of acid sites. Conversion increases with the rising temperatures from 473 K to 693 K, with an ascending rate order of Pt/SAPO-11-C < Pt/SAPO-11-T < Pt/SAPO-11-PQ. Thus, Pt/SAPO-11-PQ showed the highest activity. Selectivity for MBs continuously decreases with increasing temperature over the testing temperature region (Fig. 7b), whereas the selectivity for DBs passes through a maximum at 593 K, 613 K and 613 K for Pt/SAPO-11-C, Pt/SAPO-11-T and Pt/SAPO-11-PQ, respectively, before dropping with further temperature increase (Fig. 7c). The critical molecular diameters are 0.56 nm for 2,4-DMC$_5$ (2,4-dimethylmethylpentane) and 2,3-DMC$_5$, 0.70 nm for 2,2-DMC$_5$ and 3,3-DMC$_5$.[38] With increasing temperature, the selectivity to the four DBs increased to a maximum before they decreased with further temperature increase, as shown in Fig. S4.† In addition, the four DBs were detected in the decreasing order 2,3-DMC$_5$ > 2,4-DMC$_5$ > 2,2-DMC$_5$ > 3,3-DMC$_5$ for Pt/SAPO-11-C, Pt/SAPO-11-T and Pt/SAPO-11-PQ. The steric restrictions of the SAPO-11 pores led to a much lower selectivity for the 2,2- and 3,3-DMC$_5$, indicating confinement effects for the bulkier 2,2- and 3,3-DMC$_5$ formation. It is known that the bottleneck in the skeletal isomerization of hydrocarbons lies in the tension between highly efficient isomerization and minimal cracking,[88]
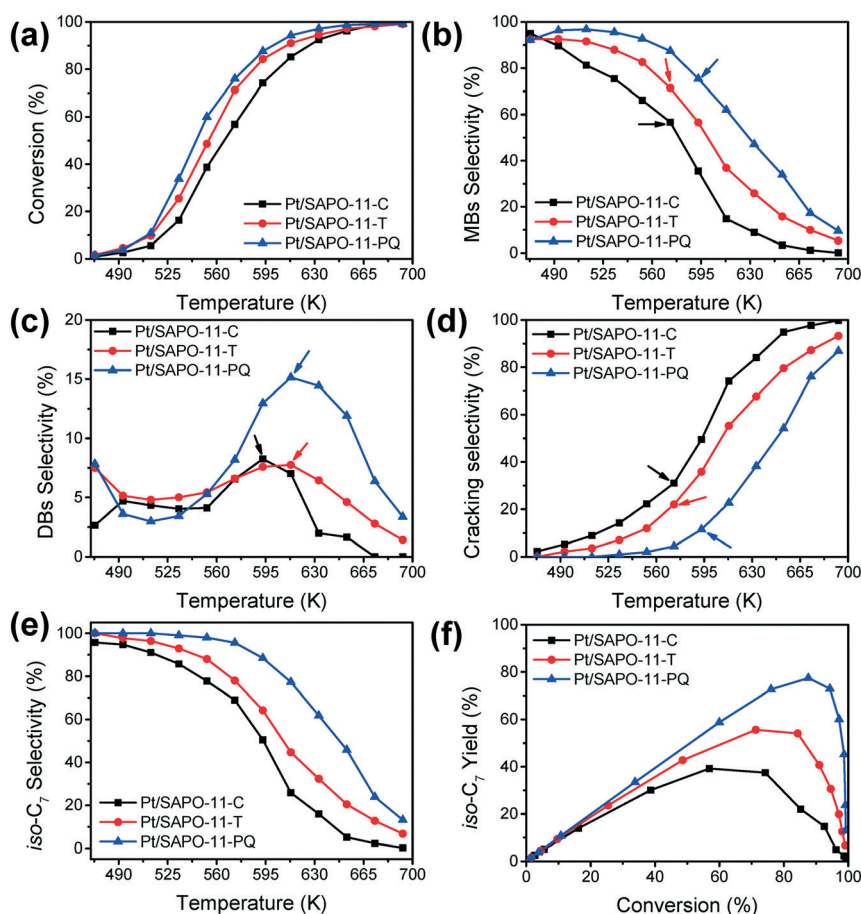

Fig. 7 Reactant conversion versus temperature (a), selectivity to MBs (b) and DBs (c) versus temperature, cracking selectivity versus temperature (d), total isomerization selectivity versus temperature (e) and total isomerization yield versus conversion (f). The arrows point to the maximum selectivity to DBs.

This journal is © The Royal Society of Chemistry 2018

Catal. Sci. Technol., 2018, **8**, 5044–5061 | 5055

so it is desirable to search for a catalyst that can efficiently reconcile this tension. As shown in Fig. 7d, compared with the Pt/SAPO-11-C catalyst, the Pt/SAPO-11-T and Pt/SAPO-11-PQ catalysts have a much lower cracking selectivity over the entire temperature range. The total isomerization selectivity decreases with increasing temperature (Fig. 7e). The selectivity for isomers is broken down into subgroups as MBs and DBs, to evaluate their respective dependence over reaction temperature. The C_7 isomers yields *vs.* reactant conversion were plotted for the catalysts in Fig. 7f. Pt/SAPO-11-PQ showed a maximum isomerization yield of 77% at a conversion of 88%. The isomerization yield for Pt/SAPO-11-T was 56% (conversion of 71%), which was much higher than that of Pt/SAPO-11-C (39%) at a conversion of 57%. The DBs can be classified into $2,2$-DMC_5, $2,4$-DMC_5, $3,3$-DMC_5 and $2,3$-DMC_5. In addition, the Pt/SAPO-11-PQ catalyst has the lowest cracking selectivity, demonstrating its remarkable advantage for the skeletal isomerization of hydrocarbons.

Diffusion measurements for hierarchical SAPO-11 crystals

In order to study the effect of mesopores on hydrocarbon diffusion in SAPO-11, 2-methylhexane, chosen as a model adsorbate, was adsorbed at 365 K. Quantification of the diffusion properties was obtained by using Fick's second law, which describes the variation of the concentration of molecules inside the zeolite channel as a function of time:[12]

$$\frac{\partial C}{\partial t} = D_{eff}\left(\frac{\partial^2 C}{\partial x^2}\right), \tag{1}$$

where C is the concentration of 2-methylhexane inside the particle, t is time, D_{eff} is the effective diffusivity, and x is the diffusion length.

At the beginning of an adsorption process in a slab-like crystal, a solution for Fick's second law is:[12,89]

$$\frac{q(t)}{q(\infty)} = \frac{2}{\sqrt{\pi}}\sqrt{\frac{D_{eff}}{L^2}}\sqrt{t}, \tag{2}$$

where $q(t)/q(\infty)$ is the normalized hydrocarbon uptake, and L is the characteristic diffusion length. The diffusion time constant, D_{eff}/L^2, can be considered as a parameter for assessing the diffusion performance of different SAPO-11 samples. Fig. 8c shows the relation between $q(t)/q(\infty)$ and diffusion time $t^{0.5}$. The D_{eff}/L^2 values calculated from the slopes of the straight line are summarized in Table 4. It can be seen that the D_{eff}/L^2 values increase as follows: SAPO-11-C < SAPO-11-T < SAPO-11-PQ. As the nanosheet's normal is along the b vector of its structure ([010]) and the unidimensional micropores run parallel to the c vector ([001]), the formation of nanosheets with large lateral size, such as for SAPO-11-T, leads to limited enhancement in the corresponding diffusion properties. On the other hand, adding PQ-10 to the synthesis markedly reduces the lateral dimension of the nanosheets,
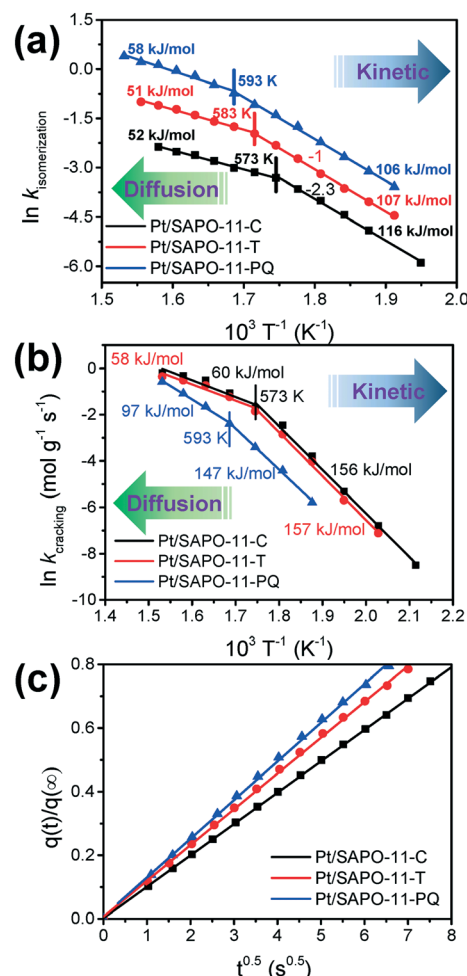

Fig. 8 Arrhenius plot of the *n*-heptane hydroconversion (shift downward by a factor of 1 and 2.3 for Pt/SAPO-11-T and Pt/SAPO-11-PQ, respectively) (a), Arrhenius plot of the formation rate for stoichiometric propane and isobutene (b) and adsorption rates of 2-methylhexane in the calcined SAPO-11 samples (c).

translating to a shortened diffusion pathway and a corresponding promotion of the diffusion properties.

Notably, the isomer selectivity for the catalysts and its increasing trend with temperature for *n*-heptane conversions obey exactly the same order. Because the Pt sites are equilibrated with surface species, the hierarchical SAPO-11 structure is responsible for the observed catalytic performance.[30] The comparable acid site density and strength, in turn, minimizes kinetic influences associated to the acid sites. One, thereby, can correlate the influence in activity and selectivity to the sole effect from diffusion properties that are governed

Table 4 The calculated values for the inverse of the diffusion time constant D/L^2 from Fig. 8c

Sample	D/L^2 (s^{-1})
SAPO-11-C	0.77×10^{-3}
SAPO-11-T	0.99×10^{-3}
SAPO-11-PQ	1.17×10^{-3}

5056 | *Catal. Sci. Technol.*, 2018, **8**, 5044–5061

This journal is © The Royal Society of Chemistry 2018

by the porous architecture. Correlating diffusion properties with isomer selectivity shows that the presence of mesopores, as well as the reduction of the crystallite size for SAPO-11 crystals can enhance the isomer selectivity as a result of the enhanced diffusion rates for isomers formed inside the micropores.

Kinetic measurements and influence of temperature and conversion levels on product distribution

The hydroisomerization of n-heptane over Pt/SAPO-11 catalyst observes a hyperboric type kinetic equation at low conversion levels (which were manipulated to be less than 10%), as shown by Noh et $al.$ for Pt supported on zeolites and by some of us.[90,91] For hydroisomerization of homologues, such as hexane[92] and octane,[37] the same kinetic law applies. When H_2/C_7 ratio is high (herein kept to 26), by approximation, the kinetic can be regarded as a pseudo-first order reaction.[91] To interpret the influence of diffusion on catalytic behaviour,[91] the effect of the temperature range over the apparent activation energies was determined through kinetic experiments. External transport limitations were ruled out by controlling the flow rate, but internal diffusion limitations could not be precluded. The apparent activation energies were obtained through the Arrhenius equation by plotting $\ln k$ $vs.$ T^{-1}, as shown in Fig. 8a. The apparent activation energy was 116 kJ mol^{-1} for Pt/SAPO-11-C between 513 K and 573 K, but the observed apparent activation energy was approximately half this value at higher temperatures (573 K to 633 K). This result confirms the findings of Höchtl et $al.$[29] In general, the presence of diffusion limitations has a strong effect on the apparent activation energy. This can be seen by expressing both the rate constant, k, and the diffusion constant, D_{eff}, in the Arrhenius form:[93]

$$k = k_0 e^{\frac{-\Delta E_{act}}{RT}} \text{ and } D_{eff} = D_0 e^{\frac{-\Delta E_{diff}}{RT}} \qquad (3)$$

In the absence of diffusion limitations, the overall activation energy is:

$$E^{app} = RT^2 \frac{\partial \ln(r)}{\partial T} = \Delta E_{act} \qquad (4)$$

However, when diffusion is important, the rate is[94]

$$R_{diff} = \eta k \left(C_s^s\right)^n \approx \frac{S}{V} \sqrt{\frac{2}{n+1} D_{eff}} k \left(C_s^s\right)^{(n+1)/2} \qquad (5)$$

which results in the following apparent activation energy

$$E^{app} = RT^2 \frac{\partial \ln(R_{diff})}{\partial T} = \frac{\Delta E_{act}}{2} + \frac{\Delta E_{diff}}{2} \approx \frac{\Delta E_{act}}{2} \text{ when } \frac{\Delta E_{diff}}{2} \to 0, \qquad (6)$$

where E^{app} is the apparent activation energy, T is the temperature, D_{eff} is the effective diffusivity, and S is the external sur-

face area of the catalyst, V is the catalyst volume, C_S^S is the reactant concentration at the catalyst surface, and k is the intrinsic reaction rate constant. Hence, the apparent activation energy is half the value one would obtain if there were no transport limitations.[93] The results thus indicate that the hydroisomerization process is limited by intrinsic reaction at low temperatures, but is limited by diffusion at higher temperatures. For Pt/SAPO-11-T and Pt/SAPO-11-PQ, activation energies of 107 kJ mol^{-1} and 106 kJ mol^{-1} were obtained below 583 K and 593 K, respectively, and approximately half of these values (51 kJ mol^{-1} and 58 kJ mol^{-1} for Pt/SAPO-11-T and Pt/SAPO-11-PQ, respectively) were obtained at higher temperatures. The trend is the same for Pt/SAPO-11-C, but the transition temperature has decreased to 573 K (Fig. 8a). Our kinetic studies show that the hierarchical architecture can expand the intrinsic reaction controlled regime towards higher temperatures, similar to our observations for other hierarchical SAPO-11 catalysts.[51]

The cracking of DBs, such as 2,3-dimethylpentane and 2,4-dimethylpentane, is regarded as the major contributor for the cracking products.[95] The kinetic data can be deduced from the catalytic evaluation results, as cracking for 2,3-dimethylpentane or 2,4-dimethylpentane is irreversible and the products are propane/propene and isobutene, as a result of β-scission (Scheme 2). The formation rates for stoichiometric quantities of propane/propene and isobutane can be used to derive the corresponding kinetic data through Arrhenius plots,[91] as displayed in Fig. 8b. The reverse reaction is negligible as well, because cracking products are thermodynamically favoured (Fig. S5†). The plots show an excellent linear relationship in the intrinsic reaction-controlled regime, where apparent activation energies for the formation of propane and isobutene cracking product are 156, 157 and 147 kJ mol^{-1}, for Pt/SAPO-11-C, Pt/SAPO-11-T and Pt/SAPO-11-PQ, respectively. These values are high, because cracking is an energetically demanding process. This explains why a low cracking product selectivity is detected for all samples within the reaction controlled regime. Conversely, a lowered activation energy of more than half the value (97 kJ mol^{-1}) of the intrinsic activation energy has been observed for Pt/SAPO-11-PQ, suggesting that the process enters an activated diffusion-controlled regime with respect to the cracking reaction, $viz.$ eqn (6). For the other two catalysts, Pt/SAPO-11-C (60 kJ mol^{-1}) and Pt/SAPO-11-PQ (58 kJ mol^{-1}), even lower activation energies can be estimated, with values close to those measured for the diffusion controlled hydroisomerization of n-heptane at similar temperatures (Fig. 8a), suggesting
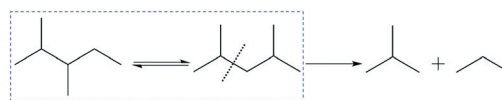
Scheme 2 Reaction network for fast dibranched isomer interconversion (inside dotted lines) and slow cracking. The formation rates of cracking products can be used to deduce cracking kinetic data by regarding dibranched isomers as a single source.

interference between the two consecutive reactions and a fast conversion from MBs to DBs. The above discussion demonstrates that, in the diffusion controlled regime, more undesired cracking products form, mainly because the diffusion of DBs is controlling the overall process, leading to a faster cracking rate as a consequence of longer residence time in the pores.

General discussion on the influence of SAPO-11 architecture on isomer selectivity

On the basis of the isomerization mechanism of *n*-alkanes over bifunctional catalysts,[96] for Pt/SAPO-11 catalysts, *n*-heptane is first dehydrogenated into *n*-heptene on Pt centres, which is fast and can be regarded as an equilibrated step. The *n*-heptene molecule diffuse and adsorb onto the B acid sites of SAPO-11 to undergo skeletal isomerization to monobranched *iso*-heptenes, which is kinetically controlling the overall reaction rate in the absence of diffusion limitations.[29,37] Sequentially, the monobranched *iso*-heptenes can be further converted into dibranched *iso*-heptenes on the B acid sites, which is known to be a kinetically fast process.[90,91] Finally, the MBs and DBs are generated after hydrogenation on Pt centres of the *iso*-heptenes to the corresponding *iso*-heptanes (Scheme 3). Cracking of DBs is responsible for the formation of lighter alkanes, but produces far less cracking products, because the process has a much higher (*e.g.*, 116 *vs.* 156 kJ mol^{-1} for SAPO-11-C) energetic barrier than isomerization in the intrinsic reaction-controlled regime. Once the reaction enters a diffusion controlled regime and diffusion becomes the rate determining step, the observed kinetics change in favor of the cracking reactions. For instance, apparent activation energies observed (52 kJ mol^{-1}) for isomerization and cracking (60 kJ mol^{-1}) become closer to each other for SAPO-11-C, leading to a loss in catalytic selectivity. This is because microporous Pt/SAPO-11-C catalyst has the largest crystallite size and the longest diffusion pathways, which leads to long residence times of dibranched *iso*-heptenes and a high cracking probability. For Pt/SAPO-11-T and Pt/SAPO-11-PQ catalysts, the smaller particles and hierarchical architecture lead to shorter residence times for dibranched *iso*-heptenes in the micropores, thereby reducing the further cracking probability. The highest isomerization yield was obtained for Pt/SAPO-11-PQ catalysts, because

SAPO-11-PQ has a more open pore structure and favorable diffusion properties. The isomer selectivity increases almost monotonically with the mass transfer properties, regardless of the relatively small difference in acidity, strongly suggesting that the isomerization selectivities are mainly affected by the pore space architecture.

One key feature for hydroisomerization is that progressively bulkier molecules are produced with the degree of skeletal isomerization. As has been shown, the diffusional behaviour and accessibility of the involved molecules influence the catalytic selectivity. Qualitative predictions of the diffusion of molecules in zeolites can be made by comparing the critical molecular diameter of the sorbates to the zeolite pore diameter.[97] Because the critical molecular diameter is 0.56 nm for MBs, which is smaller than the pore diameter (0.63 nm) of SAPO-11, but 0.70 nm for bulky DBs (such as 2,2-DMC$_5$ and 3,3-DMC$_5$), which is larger than the pore diameter of SAPO-11,[38] 2,2-DMC$_5$ and 3,3-DMC$_5$ can be formed only near the pore mouths, rather than in the microporous channels. Small DBs, such as 2,3-DMC$_5$ and 2,4-DMC$_5$ (0.56 nm), exhibit relatively insignificant diffusional retardation in SAPO-11, and can also form inside the micropores. In this respect, SAPO-11-T and SAPO-11-PQ with smaller crystallites should be beneficial to produce more DBs than SAPO-11-C.

Conclusions

In summary, we have demonstrated that oriented assembly of nanocrystallites produced from a dry gel conversion can be used to construct hierarchical architectures of SAPO-11 nanosheets. This is achieved without any additives, under tumbling crystallization conditions. Such a process opens up a new route to generate hierarchical SAPOs through changes in the stepwise crystallization process. The factor governing the formation of the nanosheets is to ensure that the inter-particle interactions are not overshadowed by gravity or Coulombic attraction. However, further inclusion of a growth modifier can be utilized to tune the architecture of the material, and a hierarchically ordered architecture featuring small crystallites and enhanced pore access can thus be achieved. Merits of such a preparation method include simplicity, low-cost, versatility and tunability. Importantly, the primary crystallite size and pore-connectivity with the exterior surface, which are key structural factors affecting diffusion properties,
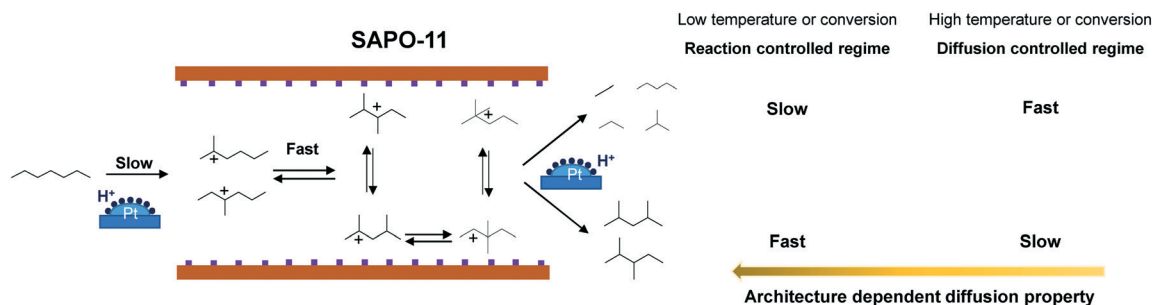
Scheme 3 Catalytic reaction sites and diffusion pathways for *n*-heptane hydroisomerization over Pt/SAPO-11 catalysts.

can be controlled. These characteristics, together with strong retained acidity, contribute to a more significant increase in isomer selectivity, owing to improved mass transfer. The proposed insights in the formation mechanism of the hierarchical architecture and associated catalytic properties are of broader significance for future catalyst designs for isomerization of *n*-paraffins.

Conflicts of interest

There are no conflicts to declare.

Acknowledgements

References

1 G. Bellussi, A. Carati and R. Millini, in *Zeolites and Catalysis*, Wiley-VCH Verlag GmbH & Co. KGaA, 2010, pp. 449–491, DOI: 10.1002/9783527630295.ch16.

2 C. Martinez and A. Corma, *Coord. Chem. Rev.*, 2011, **255**, 1558–1580.

3 Y. Li and J. Yu, *Chem. Rev.*, 2014, **114**, 7268–7316.

4 J. Kärger, *Microporous Mesoporous Mater.*, 2014, **189**, 126–135.

5 P. Kortunov, S. Vasenkov, J. Karger, R. Valiullin, P. Gottschalk, M. F. Elia, M. Perez, M. Stocker, B. Drescher, G. McElhiney, C. Berger, R. Glaser and J. Weitkamp, *J. Am. Chem. Soc.*, 2005, **127**, 13055–13059.

6 J. Kärger and D. M. Ruthven, *New J. Chem.*, 2016, **40**, 4027–4048.

7 P. Mériaudeau, V. A. Tuan, F. Lefebvre, V. T. Nghiem and C. Naccache, *Microporous Mesoporous Mater.*, 1998, **22**, 435–449.

8 A. K. Sinha and S. Sivasanker, *Catal. Today*, 1999, **49**, 293–302.

9 P. Liu, J. Ren and Y. Sun, *Catal. Commun.*, 2008, **9**, 1804–1809.

10 A. Patrigeon, E. Benazzi, C. Travers and J. Y. Bernhard, *Catal. Today*, 2001, **65**, 149–155.

11 L. Guo, Y. Fan, X. J. Bao, G. Shi and H. Y. Liu, *J. Catal.*, 2013, **301**, 162–173.

12 M. Y. Kim, K. Lee and M. Choi, *J. Catal.*, 2014, **319**, 232–238.

13 Y. Fan, H. Xiao, G. Shi, H. Liu and X. Bao, *J. Catal.*, 2012, **285**, 251–259.

14 E. P. Parry, *J. Catal.*, 1963, **2**, 371–379.

15 S. J. Miller, in *Stud. Surf. Sci. Catal.*, ed. H. G. K. H. P. J. Weitkamp and W. Hölderich, Elsevier, 1994, vol. 84, pp. 2319–2326.

16 R. J. Taylor and R. H. Petty, *Appl. Catal., A*, 1994, **119**, 121–138.

17 J. M. Campelo, F. Lafont and J. M. Marinas, *Appl. Catal., A*, 1998, **170**, 139–144.

18 V. Calemma, S. Peratello and C. Perego, *Appl. Catal., A*, 2000, **190**, 207–218.

19 Y. Rezgui and M. Guemini, *Energy Fuels*, 2007, **21**, 602–609.

20 L. Guo, X. Bao, Y. Fan, G. Shi, H. Liu and D. Bai, *J. Catal.*, 2012, **294**, 161–170.

21 K.-C. Park and S.-K. Ihm, *Appl. Catal., A*, 2000, **203**, 201–209.

22 C. M. Lopez, Y. Guillen, L. Garcia, L. Gomez and A. Ramirez, *Catal. Lett.*, 2008, **122**, 267–273.

23 J. A. Martens, W. Souverijns, W. Verrelst, R. Parton, G. F. Froment and P. A. Jacobs, *Angew. Chem., Int. Ed. Engl.*, 1995, **34**, 2528–2530.

24 M. C. Claude, G. Vanbutsele and J. A. Martens, *J. Catal.*, 2001, **203**, 213–231.

25 M. A. Arribas, F. Márquez and A. Martínez, *J. Catal.*, 2000, **190**, 309–319.

26 E. Blomsma, J. A. Martens and P. A. Jacobs, *J. Catal.*, 1996, **159**, 323–331.

27 Z. B. Wang, A. Kamo, T. Yoneda, T. Komatsu and T. Yashima, *Appl. Catal., A*, 1997, **159**, 119–132.

28 J. N. Kondo, S. W. Yang, Q. J. Zhu, S. Inagaki and K. Domen, *J. Catal.*, 2007, **248**, 53–59.

29 M. Höchtl, A. Jentys and H. Vinek, *J. Catal.*, 2000, **190**, 419–432.

30 T. L. M. Maesen, M. Schenk, T. J. H. Vlugt, J. P. d. Jonge and B. Smit, *J. Catal.*, 1999, **188**, 403–412.

31 G. Sastre, A. Chica and A. Corma, *J. Catal.*, 2000, **195**, 227–236.

32 P. Raybaud, A. Patrigeon and H. Toulhoat, *J. Catal.*, 2001, **197**, 98–112.

33 M. Höchtl, A. Jentys and H. Vinek, *Catal. Today*, 2001, **65**, 171–177.

34 Y. Seo, S. Lee, C. Jo and R. Ryoo, *J. Am. Chem. Soc.*, 2013, **135**, 8806–8809.

35 Y. Liu, W. Qu, W. Chang, S. Pan, Z. Tian, X. Meng, M. Rigutto, A. v. d. Made, L. Zhao, X. Zheng and F.-S. Xiao, *J. Colloid Interface Sci.*, 2014, **418**, 193–199.

36 F. Zhang, Y. Liu, Q. Sun, Z. Dai, H. Gies, Q. Wu, S. Pan, C. Bian, Z. Tian, X. Meng, Y. Zhang, X. Zou, X. Yi, A. Zheng, L. Wang and F.-S. Xiao, *Chem. Commun.*, 2017, **53**, 4942–4945.

37 A. Chica and A. Corma, *Chem. Ing. Tech.*, 2007, **79**, 857–870.

38 J. M. Campelo, F. Lafont and J. M. Marinas, *J. Catal.*, 1995, **156**, 11–18.

39 S. Lin, J. Y. Li, R. P. Sharma, J. H. Yu and R. R. Xu, *Top. Catal.*, 2010, **53**, 1304–1310.

40 K. Möller, B. Yilmaz, R. M. Jacubinas, U. Müller and T. Bein, *J. Am. Chem. Soc.*, 2011, **133**, 5284–5295.

41 J. Chen, W. Hua, Y. Xiao, Q. Huo, K. Zhu and X. Zhou, *Chem. – Eur. J.*, 2014, **20**, 14744–14755.

42 M. Musa, D. M. Dawson, S. E. Ashbrook and R. E. Morris, *Microporous Mesoporous Mater.*, 2017, **239**, 336–341.

43 H. van Heyden, S. Mintova and T. Bein, *Chem. Mater.*, 2008, **20**, 2956–2963.

This journal is © The Royal Society of Chemistry 2018

Catal. Sci. Technol., 2018, **8**, 5044–5061 | 5059

44 M. Vilaseca, S. Mintova, K. Karaghiosoff, T. H. Metzger and T. Bein, *Catal. Today*, 2004, **226**, 1–6.

45 T. M. Davis, T. O. Drews, H. Ramanan, C. He, J. S. Dong, H. Schnablegger, M. A. Katsoulakis, E. Kokkoli, A. V. McCormick, R. L. Penn and M. Tsapatsis, *Nat. Mater.*, 2006, **5**, 400–408.

46 M. Kumar, H. Luo, Y. Roman-Leshkov and J. D. Rimer, *J. Am. Chem. Soc.*, 2015, **137**, 13007–13017.

47 J. W. Zheng, W. P. Zhang, Z. T. Liu, Q. S. Huo, K. K. Zhu, X. G. Zhou and W. K. Yuan, *Microporous Mesoporous Mater.*, 2016, **225**, 74–87.

48 K. K. Zhu, J. M. Sun, J. Liu, L. Q. Wang, H. Y. Wan, J. Z. Hu, Y. Wang, C. H. F. Peden and Z. M. Nie, *ACS Catal.*, 2011, **1**, 682–690.

49 W. Song, Z. T. Liu, L. P. Liu, A. L. Skov, N. Song, G. Xiong, K. K. Zhu and X. G. Zhou, *RSC Adv.*, 2015, **5**, 31195–31204.

50 K. K. Zhu and X. G. Zhou, *Curr. Opin. Chem. Eng.*, 2015, **9**, 42–48.

51 D. Jin, G. Ye, J. Zheng, W. Yang, K. Zhu, M.-O. Coppens and X. Zhou, *ACS Catal.*, 2017, **7**, 5887–5902.

52 D. Jin, Z. Liu, J. Zheng, W. Hua, J. Chen, K. Zhu and X. Zhou, *RSC Adv.*, 2016, **6**, 32523–32533.

53 T. Onfroy, G. Clet and M. Houalla, *Microporous Mesoporous Mater.*, 2005, **82**, 99–104.

54 C. A. Emeis, *J. Catal.*, 1993, **141**, 347–354.

55 F. D. Wang, V. N. Richards, S. P. Shields and W. E. Buhro, *Chem. Mater.*, 2014, **26**, 5–21.

56 J. Lee, J. Yang, S. G. Kwon and T. Hyeon, *Nat. Rev. Mater.*, 2016, **1**, 16034.

57 V. K. LaMer and R. H. Dinegar, *J. Am. Chem. Soc.*, 1950, **72**, 4847–4854.

58 P. V. Kortunov, L. Heinke, M. Arnold, Y. Nedellec, D. J. Jones, J. Caro and J. Karger, *J. Am. Chem. Soc.*, 2007, **129**, 8041–8047.

59 M. Milina, S. Mitchell, P. Crivelli, D. Cooke and J. Pérez-Ramírez, *Nat. Commun.*, 2014, **5**, 3922.

60 A. I. Lupulescu, M. Kumar and J. D. Rimer, *J. Am. Chem. Soc.*, 2013, **135**, 6608–6617.

61 S. Zhang, S.-L. Chen, P. Dong, G. Yuan and K. Xu, *Appl. Catal., A*, 2007, **332**, 46–55.

62 Y. Fan, D. Lei, G. Shi and X. Bao, *Catal. Today*, 2006, **114**, 388–396.

63 H. Cölfen and M. Antonietti, *Angew. Chem., Int. Ed.*, 2005, **44**, 5576–5591.

64 Q. Wu, I. Nartey Oduro, Y. Huang and Y. Fang, *Microporous Mesoporous Mater.*, 2015, **218**, 24–32.

65 J. C. Groen, L. A. A. Peffer and J. Pérez-Ramírez, *Microporous Mesoporous Mater.*, 2003, **60**, 1–17.

66 S. Zhang, S.-L. Chen and P. Dong, *Catal. Lett.*, 2010, **136**, 126–133.

67 Y. Liu and R. L. Withers, *J. Solid State Chem.*, 2003, **172**, 431–437.

68 L. Karwacki, E. Stavitski, M. H. F. Kox, J. Kornatowski and B. M. Weckhuysen, *Angew. Chem., Int. Ed.*, 2007, **46**, 7228–7231.

69 E. Stavitski, M. R. Drury, D. A. M. de Winter, M. H. F. Kox and B. M. Weckhuysen, *Angew. Chem., Int. Ed.*, 2008, **47**, 5637–5640.

70 D. Verboekend, M. Milina and J. Pérez-Ramírez, *Chem. Mater.*, 2014, **26**, 4552–4562.

71 M. Choi, K. Na, J. Kim, Y. Sakamoto, O. Terasaki and R. Ryoo, *Nature*, 2009, **461**, 246–U120.

72 D. Xu, Y. Ma, Z. Jing, L. Han, B. Singh, J. Feng, X. Shen, F. Cao, P. Oleynikov, H. Sun, O. Terasaki and S. Che, *Nat. Commun.*, 2014, **5**, 4262.

73 A. Buchholz, W. Wang, M. Xu, A. Arnold and M. Hunger, *Microporous Mesoporous Mater.*, 2002, **56**, 267–278.

74 M. Briend, M. J. Peltre, A. Lamy, P. P. Man and D. Barthomeuf, *J. Catal.*, 1992, **138**, 90–100.

75 P. Mériaudeau, V. A. Tuan, V. T. Nghiem, S. Y. Lai, L. N. Hung and C. Naccache, *J. Catal.*, 1997, **169**, 55–66.

76 Y. Watanabe, A. Koiwai, H. Takeuchi, S. A. Hyodo and S. Noda, *J. Catal.*, 1993, **143**, 430–436.

77 H. Zubowa, E. Alsdorf, R. Fricke, F. Neissendorfer, J. Richter-Mendau, E. Schreier, D. Zeigan and B. Zibrowius, *J. Chem. Soc., Faraday Trans.*, 1990, **86**, 2307–2312.

78 P. Liu, J. Ren and Y. Sun, *Microporous Mesoporous Mater.*, 2008, **114**, 365–372.

79 L. Zhang, J. Bates, D. Chen, H.-Y. Nie and Y. Huang, *J. Phys. Chem. C*, 2011, **115**, 22309–22319.

80 T. Blasco, A. Chica, A. Corma, W. J. Murphy, J. Agúndez-Rodríguez and J. Pérez-Pariente, *J. Catal.*, 2006, **242**, 153–161.

81 G. Sastre, D. W. Lewis and C. R. A. Catlow, *J. Mol. Catal. A: Chem.*, 1997, **119**, 349–356.

82 J. A. Martens, P. J. Grobet and P. A. Jacobs, *J. Catal.*, 1990, **126**, 299–305.

83 T. Masukawa, T. Komatsu and T. Yashima, *Zeolites*, 1997, **18**, 10–17.

84 J. A. Z. Pieterse, S. Veefkind-Reyes, K. Seshan, L. Domokos and J. A. Lercher, *J. Catal.*, 1999, **187**, 518–520.

85 Y. Fan, H. Xiao, G. Shi, H. Liu, Y. Qian, T. Wang, G. Gong and X. Bao, *J. Catal.*, 2011, **279**, 27–35.

86 F. Thibault-Starzyk, A. Vimont and J.-P. Gilson, *Catal. Today*, 2001, **70**, 227–241.

87 F. Thibault-Starzyk, I. Stan, S. Abello, A. Bonilla, K. Thomas, C. Fernandez, J. P. Gilson and J. Perez-Ramirez, *J. Catal.*, 2009, **264**, 11–14.

88 V. M. Akhmedov and S. H. Al-Khowaiter, *Catal. Rev.: Sci. Eng.*, 2007, **49**, 33–139.

89 J. C. Groen, W. Zhu, S. Brouwer, S. J. Huynink, F. Kapteijn, J. A. Moulijn and J. Pérez-Ramírez, *J. Am. Chem. Soc.*, 2007, **129**, 355–360.

90 G. Noh, Z. Shi, S. I. Zones and E. Iglesia, *J. Catal.*, 2018, DOI: 10.1016/j.jcat.2018.03.033.

91 T. Yue, W. Liu, L. Li, X. Zhao, K. Zhu, X. Zhou and W. Yang, *J. Catal.*, 2018, **364**, 308–327.

92 J. Macht, R. T. Carr and E. Iglesia, *J. Am. Chem. Soc.*, 2009, **131**, 6554–6565.

93 I. Chorkendorff and J. W. Niemantsverdriet, in *Concepts of Modern Catalysis and Kinetics*, Wiley-VCH Verlag

5060 | *Catal. Sci. Technol.*, 2018, **8**, 5044–5061

This journal is © The Royal Society of Chemistry 2018

GmbH & Co. KGaA, 2005, pp. 167–214, DOI: 10.1002/3527602658.ch5.

94 G. F. Froment and K. B. Bischoff, *Chemical Reactor Analysis Design*, 1990.

95 P. Raybaud, A. Patrigeon and H. Toulhoat, *J. Catal.*, 2001, **197**, 98–112.

96 Y. Ono, *Catal. Today*, 2003, **81**, 3–16.

97 V. R. Choudhary and D. B. Akolekar, *J. Catal.*, 1989, **117**, 542–548.

This journal is © The Royal Society of Chemistry 2018

Catal. Sci. Technol., 2018, **8**, 5044–5061 | 5061